Conference Proceedings of the Society for Experimental Mechanics Series

Randy Mayes · Daniel Rixen · Matt Allen *Editors*

Topics in Experimental Dynamic Substructuring, Volume 2

Proceedings of the 31st IMAC, A Conference on Structural Dynamics, 2013

SEM

Springer

Conference Proceedings of the Society for Experimental Mechanics Series

Series Editor
Tom Proulx
Society for Experimental Mechanics, Inc.,
Bethel, CT, USA

For further volumes:
http://www.springer.com/series/8922

Randy Mayes • Daniel Rixen • Matt Allen
Editors

Topics in Experimental Dynamic Substructuring, Volume 2

Proceedings of the 31st IMAC, A Conference on Structural Dynamics, 2013

Springer

Editors
Randy Mayes
Sandia National Laboratories
Albuquerque, NM, USA

Matt Allen
Engineering Physics Department
University of Wisconsin Madison
Madison, WI, USA

Daniel Rixen
Department of Precision and Microsystems Engineering
Delft University of Technology
Delft, Netherlands

ISSN 2191-5644 ISSN 2191-5652 (electronic)
ISBN 978-1-4614-6539-3 ISBN 978-1-4614-6540-9 (eBook)
DOI 10.1007/978-1-4614-6540-9
Springer New York Heidelberg Dordrecht London

Library of Congress Control Number: 2013939185

Printed on acid-free paper

Springer is part of Springer Science+Business Media (www.springer.com)

Preface

Topics in Experimental Dynamic Substructuring, Volume 2: Proceedings of the 31st IMAC, A Conference on Structural Dynamics, 2013 represents one of the seven volumes of technical papers presented at the 31st IMAC, a conference and exposition on structural dynamics, 2013, organized by the Society for Experimental Mechanics and held in Garden Grove, California, from February 11 to 14, 2013. The full proceedings also include volumes on nonlinear dynamics; dynamics of bridges; dynamics of civil structures; model validation and uncertainty quantification; special topics in structural dynamics; and modal analysis.

Each collection presents early findings from experimental and computational investigations on an important area within structural dynamics. Substructuring is one of these areas.

Substructuring is a general paradigm in engineering dynamics where a complicated system is analyzed by considering the dynamic interactions between subcomponents. In numerical simulations, substructuring allows one to reduce the complexity of parts of the system in order to construct a computationally efficient model of the assembled system. A subcomponent model can also be derived experimentally, allowing one to predict the dynamic behavior of an assembly by combining experimentally and/or analytically derived models. This can be advantageous for subcomponents that are expensive or difficult to model analytically. Substructuring can also be used to couple numerical simulation with real-time testing of components. Such approaches are known as hardware-in-the-loop or hybrid testing.

Whether experimental or numerical, all substructuring approaches have a common basis, namely the equilibrium of the substructures under the action of the applied and interface forces and the compatibility of displacements at the interfaces of the subcomponents. Experimental substructuring requires special care in the way the measurements are obtained and processed in order to assure that measurement inaccuracies and noise do not invalidate the results. In numerical approaches, the fundamental quest is the efficient computation of reduced order models describing the substructure's dynamic motion. For hardware-in-the-loop applications difficulties include the fast computation of the numerical components and the proper sensing and actuation of the hardware component. Recent advances in experimental techniques, sensor/actuator technologies, novel numerical methods, and parallel computing have rekindled interest in substructuring in recent years, leading to new insights and improved experimental and analytical techniques.

The organizers would like to thank the authors, presenters, session organizers, and session chairs for their participation in this track.

Albuquerque, NM, USA — Randy Mayes
Delft, Netherlands — Daniel Rixen
Madison, WI, USA — Matt Allen

Contents

Chapter 1
Integrating Biodynamic Measurements in Frequency-Based Substructuring to Study Human-Structure Interaction

Sébastien Perrier, Yvan Champoux, and Jean-Marc Drouet

Abstract The mechanical behavior of the human body has long been characterized using biodynamic measurements on various human body parts in several positions and postures. Generally, these measurements are gathered as close as possible to the skin-mechanical structure interface for best results understanding how the body reacts when in contact with a vibrating structure. Substructuring methods have been widely used on mechanical structures to study and improve the dynamic behavior of complex assemblies. In the case of interactions between a human body and a vibrating structure, the dynamics involved in the structure alone is as important as the dynamics of the human body. Thus, the use of Frequency-Based Substructuring (FBS) to combine biodynamic measurements with the structure's dynamic behavior is essential to understanding the vibration transmission phenomena in this complex assembly.

This article presents the advantages of this approach as well as the challenges when performing FBS between a mechanical structure and biodynamic measurements. The study focuses on a vibrating handlebar in conjunction with 3 different holding positions of the hand-arm system. The FBS assemblies are gathered and the results are compared with experimental measurements on the entire assembled structure for each position over a frequency range between 1 and 100 Hz.

Keywords Biodynamics • Substructuring • Human-structure interaction • Experimental measurements • Structural dynamics

1.1 Introduction

The mechanical behavior of the human body under vibration has long been characterized and studied in the context of health and safety, as well as in the context of dynamic comfort evaluation. Among them, whole-body vibration and hand-transmitted vibration have been studied the most in order to minimize the undesirable effects of vibration [1–19]. Hand-transmitted vibration is of great interest since the hands are highly sensitive in capturing vibration discomfort and high levels of hand vibration can even be detrimental to overall health.

The characterization of hand-transmitted vibration (HTV) depends on several parameters such as vibration frequency and magnitudes, axis of vibration, coupling forces, frequency weighting, and others. For example in ISO-5349 [13], which documents the measurement, the dose–response relationship, and the weighting filter for assessment of HTV, the current weighting function proposed significantly suppresses the magnitude of vibration at frequencies above 100 Hz. The dynamic response behavior of the hand-arm system can be described as *through-the-hand-arm* and *to-the-hand* response functions. The *through-the-hand-arm* response function describes the transmission of vibration as the ratio of the motion magnitude at a specific segment of the hand-arm to that at the hand-handle interface. The biodynamic response in terms of the *to-the-hand* function relates the vibration in the vicinity of the hand to the force at the driving point [7]. The *to-the-hand* dynamic response behavior is the one to use when studying humans in contact with vibrating structures. This biodynamic response behavior has been extensively investigated, but the majority of the studies are based upon either the absorbed power or the driving point mechanical impedance Z (DPMI). These two expressions are relatively similar. The DPMI is computed from

S. Perrier (✉) • Y. Champoux • J.-M. Drouet
Department of Mechanical Engineering, VélUS, Université de Sherbrooke, 2500 boul. de l'Université, Sherbrooke, QC, Canada J1K 2R1
e-mail: Sebastien.Perrier@USherbrooke.ca

R. Mayes et al. (eds.), *Topics in Experimental Dynamic Substructuring, Volume 2: Proceedings of the 31st IMAC, A Conference on Structural Dynamics, 2013*, Conference Proceedings of the Society for Experimental Mechanics Series 36,
DOI 10.1007/978-1-4614-6540-9_1,

the force F – velocity v relationship at the driving point, as described in Eq. (1.1), and the vibration power at the driving point is computed from the parameters used in calculating the DPMI, as described in Eq. (1.2).

$$Z\left(j\omega\right)=\frac{F\left(j\omega\right)}{v\left(j\omega\right)} \tag{1.1}$$

$$P\left(\omega\right)=\mathrm{Re}\left[Z\left(j\omega\right)\right]\left|v\left(j\omega\right)\right|^{2} \tag{1.2}$$

where v is the root-mean-square value of the velocity at the same frequency.

The biodynamic response characteristics of the human hand-arm have been measured on human subjects under carefully controlled conditions to control several parameters such as posture, hand position, type of excitation, excitation direction, push and grip forces [2–6]. Nonetheless, considerable differences are known to exist in the measured data reported by investigators. These differences have been partially attributed to variations in intrinsic and extrinsic variables, test conditions, methodologies employed in the various studies [1], and the dynamic behavior of the handle itself [8, 15].

With difficulties to obtain repetitive measurements involving representative human-subject samples and test conditions due to inter- and intrasubject variabilities, biodynamic models of the hand and arm have been proposed to characterize vibration amplitude and power flow in the coupled hand, structure, and workpiece system. The majority of the reported models are mechanical models that comprise lumped mass, stiffness, and damping elements in which the lumped parameter values are identified upon the curve fitting of the measured data.

The models, therefore, do not adequately represent the biomechanical properties of the human hand and arm [7]. Furthermore, the models characterize the uncoupled biodynamic behavior of the hand and arm along the three independent orthogonal axes of vibration. All the models thus neglect to consider the dynamic coupling effects of the hand and arm.

Owing to the complex nature of the structure vibration and coupled hand-structure system dynamics, the approach developed in this work is to consider the hand-arm system as a “black box”. Its dynamic response with measured DPMI can be described, and these characteristics assembled with those of the structure by a substructuring method to develop a coupling model for the study of human–structure interactions.

Substructuring methods have become a focus of research in structural dynamics [20–30] and have been used on mechanical structures to study and improve the dynamic behavior of complex assemblies. Whereas knowledge of the interactions between structure assemblies has been a major concern in mechanical engineering since the 1960s, studies of human–structure interactions in mechanics are sparsely documented in comparison.

To the authors’ knowledge, the first attempt to study a substructuring coupling that involves both the human body and a mechanical structure was made by the authors themselves [31]. No human-structure interactions using the Frequency-Based Substructuring (FBS) method have been explored since that time. In contact with a human body part, the dynamic behavior of a lightweight structure changes radically from its original uncoupled condition. Therefore, the use of FBS to combine biodynamic measurements with the structure’s dynamic behavior is essential to understand vibration transmission phenomena.

In this work, we present the advantages of this approach as well as the challenges when performing FBS using computed characteristics of the mechanical structure and biodynamic measurements. The FBS method allows coupling between substructures through consideration of their interface set only [26]. This is a major advantage in linking a mechanical structure with the human body where only interface measurements can be gathered. The study focuses on the hand-arm in conjunction with a vibrating structure in 3 different positions. Although the human body is not linear, mechanical coupling using the FBS method can be used with the hand-arm system by controlling various parameters [31]. Each substructure is characterized in the frequency range [1, 100] Hz. The mechanical structure is characterized by the mechanical mobility Frequency Response Function (FRF) using a Finite Elements model and the hand-arm by measured mechanical impedance FRF. Finite Elements (FE) are used to characterize the mechanical structure since all the mechanical information, as well as the translational and rotational degrees of freedom, are intrinsically available. The hybrid FBS assemblies are then gathered and the results are compared with experimental measurements over the entire assembled structure for each position.

1.2 Methods

The methods used in this paper to join the human hand-arm with a mechanical structure include the generalized frequency domain substructure synthesis presented in [26]. This well-known method, also referred to as FBS (Frequency-Based Substructuring), combines the response FRF data of each substructure to analyze the dynamics of a complex assembled structure. It enables substructures to be coupled by taking into account the characteristics of the interface nodes only. It can also utilize experimentally derived data effectively in combination with finite element results. This method is based on an implicit statement of the force and velocity continuity considerations at the connection nodes. It leads to the mathematical expression for the FRF coupling of two substructures in terms of mobility Y (velocity/force) shown in Eq. (1.3) where: a and b identify the two substructures involved; A is the set of internal degrees of freedom in substructure a; I is the interface contact set between substructures a and b; and B is the set of internal degrees of freedom in substructure b.

$$\begin{bmatrix} \mathbf{Y}_{AA} & \mathbf{Y}_{AI} & \mathbf{Y}_{AB} \\ \mathbf{Y}_{IA} & \mathbf{Y}_{II} & \mathbf{Y}_{IB} \\ \mathbf{Y}_{BA} & \mathbf{Y}_{BI} & \mathbf{Y}_{BB} \end{bmatrix}^{ab} = \begin{bmatrix} \mathbf{Y}^a_{AA} & \mathbf{Y}^a_{AI} & 0 \\ \mathbf{Y}^a_{IA} & \mathbf{Y}^a_{II} & 0 \\ 0 & 0 & \mathbf{Y}^b_{BB} \end{bmatrix} - \begin{Bmatrix} \mathbf{Y}^a_{AI} \\ \mathbf{Y}^a_{II} \\ -\mathbf{Y}^b_{BI} \end{Bmatrix} \left[\mathbf{Y}^a_{II} + \mathbf{Y}^b_{II}\right]^{-1} \begin{Bmatrix} \mathbf{Y}^a_{IA} \\ \mathbf{Y}^a_{II} \\ -\mathbf{Y}^b_{IB} \end{Bmatrix}^{\mathrm{T}} \tag{1.3}$$

Substructures a and b represent the mechanical structure and the hand-arm, respectively. The coupling process using the FBS method is achieved by computing the mechanical structure mobility characteristics from the FE model and by measuring the impedance at the hands. These characteristics are assembled through Eq. (1.3) to predict the assembly's dynamic behavior. The mobility characteristics of the assembly are then compared with the measured mobility characteristics of the mechanical structure in contact with both hands. For this study, only interface data can be gathered for the hand-arm system, and therefore the equation can be simplified as shown in Eq. (1.4).

$$\begin{bmatrix} \mathbf{Y}_{AA} & \mathbf{Y}_{AI} \\ \mathbf{Y}_{IA} & \mathbf{Y}_{II} \end{bmatrix}^{ab} = \begin{bmatrix} \mathbf{Y}^a_{AA} & \mathbf{Y}^a_{AI} \\ \mathbf{Y}^a_{IA} & \mathbf{Y}^a_{II} \end{bmatrix} - \begin{Bmatrix} \mathbf{Y}^a_{AI} \\ \mathbf{Y}^a_{II} \end{Bmatrix} \left[\mathbf{Y}^a_{II} + \mathbf{Y}^b_{II}\right]^{-1} \begin{Bmatrix} \mathbf{Y}^a_{IA} \\ \mathbf{Y}^a_{II} \end{Bmatrix}^{\mathrm{T}} \tag{1.4}$$

Since the measurements of the mobility characteristics are made on the mechanical structure in contact with both hands, we are focusing only on the mechanical mobility determined by an excitation force applied at the internal set A for the substructure a and a velocity response at the interface set I.

$$\left[\mathbf{Y}^{ab}_{IA}\right] = \left[\mathbf{Y}^a_{IA}\right] - \left[\mathbf{Y}^a_{II}\right]\left[\mathbf{Y}^a_{II} + \mathbf{Y}^b_{II}\right]^{-1}\left[\mathbf{Y}^a_{IA}\right] \tag{1.5}$$

Equation (1.5) can be developed to reveal the left and right hands interface points, respectively, *I1* and *I2*.

$$\begin{bmatrix} \mathbf{Y}^{ab}_{I1A} \\ \mathbf{Y}^{ab}_{I2A} \end{bmatrix} = \begin{bmatrix} \mathbf{Y}^a_{I1A} \\ \mathbf{Y}^a_{I2A} \end{bmatrix} - \begin{bmatrix} \mathbf{Y}^a_{I1I1} & \mathbf{Y}^a_{I1I2} \\ \mathbf{Y}^a_{I2I1} & \mathbf{Y}^a_{I2I2} \end{bmatrix} \left[\begin{bmatrix} \mathbf{Y}^a_{I1I1} & \mathbf{Y}^a_{I1I2} \\ \mathbf{Y}^a_{I2I1} & \mathbf{Y}^a_{I2I2} \end{bmatrix} + \begin{bmatrix} \mathbf{Y}^b_{I1I1} & \mathbf{Y}^b_{I1I2} \\ \mathbf{Y}^b_{I2I1} & \mathbf{Y}^b_{I2I2} \end{bmatrix}\right]^{-1} \begin{bmatrix} \mathbf{Y}^a_{I1A} \\ \mathbf{Y}^a_{I2A} \end{bmatrix} \tag{1.6}$$

Furthermore, assumption is made that left and right hands are dynamically independent.

$$\begin{bmatrix} \mathbf{Y}^{ab}_{I1A} \\ \mathbf{Y}^{ab}_{I2A} \end{bmatrix} = \begin{bmatrix} \mathbf{Y}^a_{I1A} \\ \mathbf{Y}^a_{I2A} \end{bmatrix} - \begin{bmatrix} \mathbf{Y}^a_{I1I1} & \mathbf{Y}^a_{I1I2} \\ \mathbf{Y}^a_{I2I1} & \mathbf{Y}^a_{I2I2} \end{bmatrix} \left[\begin{bmatrix} \mathbf{Y}^a_{I1I1} & \mathbf{Y}^a_{I1I2} \\ \mathbf{Y}^a_{I2I1} & \mathbf{Y}^a_{I2I2} \end{bmatrix} + \begin{bmatrix} \mathbf{Y}^b_{I1I1} & 0 \\ 0 & \mathbf{Y}^b_{I2I2} \end{bmatrix}\right]^{-1} \begin{bmatrix} \mathbf{Y}^a_{I1A} \\ \mathbf{Y}^a_{I2A} \end{bmatrix} \tag{1.7}$$

1.2.1 Target Measurements

These measurements are used to evaluate the accuracy of the FBS prediction for the mechanical structure coupled with both hands (Eq. (1.7)). The mechanical structure is an aluminum assembly composed of a handlebar, a stem and a support. Figure 1.1 shows the structure installed on an excitation device used to gather target measurements with both hands on the structure. This excitation device is a hydraulic excitation system able to handle important loads and designed to produce a vertical excitation. Only the vertical Z-axis is presented in this paper.

To get the mobility of this assembly (structure with hands on it), the excitation is characterized using a six degrees of freedom (DOFs) forces/moments sensor (AMTI MC3A-500) installed between the excitation device and the support, and an accelerometer is fixed to the handlebar as close as possible to the hands. The velocity is obtained by integrating the acceleration in the frequency domain. A vibration signal reproducing the dynamic characteristics of a road is provided to the excitation system [32]. The acquisition system is a LMS SCADAS Recorder using Test.Lab 12A software.

Three postures of the hand-arm leaning on the structure are tested (Fig. 1.2). Each of them requires that the arms be kept straight. For each posture, the subject is asked to hold the handle without applying any grip force, just leaning on the structure. The push force applied by the subject on the structure is measured to control the posture during acquisition. The subject is asked to maintain a constant push force during the test using the DC values displayed by the 6DOFs forces/moments sensor in the X and Z axes. For each posture, the DC values along X and Z axes are recorded for further use during the measurement of the hand-arm mechanical impedance.

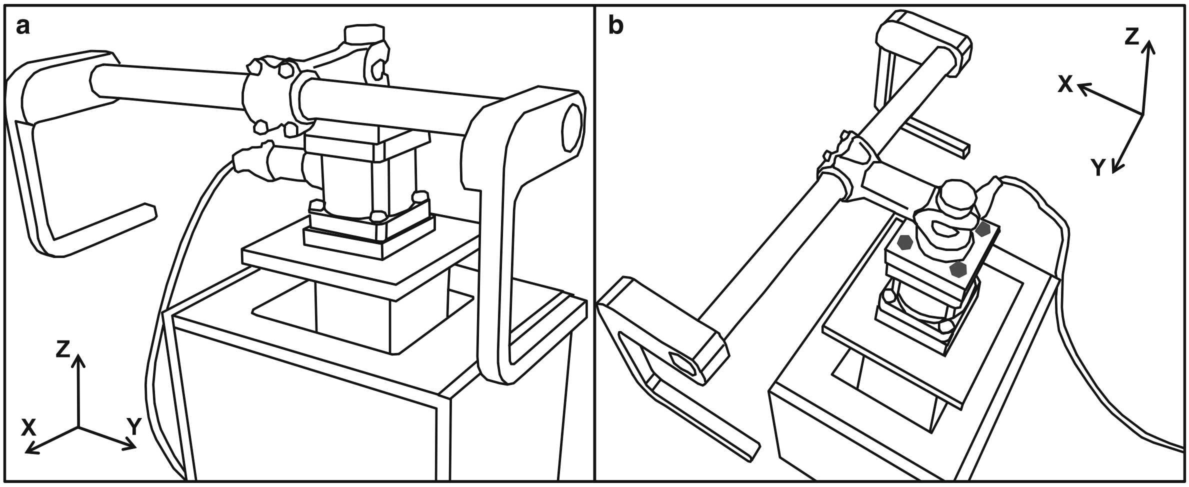

Fig. 1.1 Mechanical assembly with the 6DOFs forces/moments sensor installed on the excitation device. (**a**) *Front view*, (**b**) *Top view*

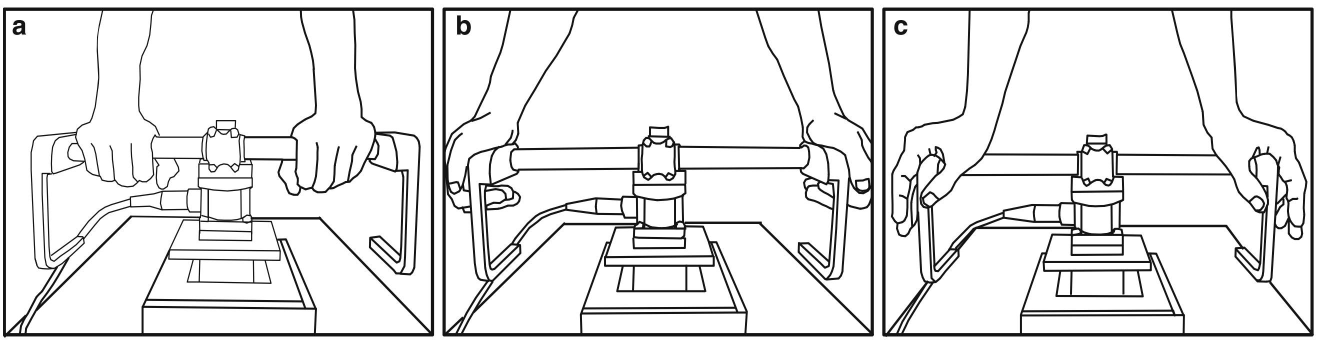

Fig. 1.2 Three test postures for the hands on the mechanical assembly. (**a**) Posture with DC values X: 10 N and Z: −70 N. (**b**) Posture with DC values X: 15 N and Z: −85 N. (**c**) Posture with DC values X: 25 N and Z: −105 N

1.2.2 Hand-Arm Mechanical Impedance

In Eq. (1.7), $\boldsymbol{Y}_{I1I1}{}^{b}$ corresponds to the matrix mobility for the left hand-arm system and $\boldsymbol{Y}_{I2I2}{}^{b}$ corresponds to the matrix mobility for the right hand-arm system. In these two matrices, only the term corresponding to an excitation and response along the vertical Z-axis is retained.

Typically, the dynamic characteristics of the hand-arm are in the form of mechanical impedance. For this reason and in this study, the hand-arm is characterized in terms of measured impedance. Theoretically, the mobility also known as admittance is the inverse of the impedance $\left([\mathbf{Y}] = [\mathbf{Z}]^{-1}\right)$.

The mechanical impedance of the hand-arm is obtained using two specially designed handles. One has a cylindrical body and the other one has a shape that is as close as possible to the shape of the assembly handlebar. For each measurement, the handle is equipped with an accelerometer and is mounted on the 6 DOFs forces/moments sensor installed on the same excitation device as for the target measurements (Fig. 1.3). The same LMS system is used as a signal generator and the dynamic characteristics of the road are provided to the excitation system.

Measurements are performed with and without a hand on the handle. Because the handles are sufficiently rigid in the frequency range of interest, the handle impedance can then be subtracted from the total impedance (hand + handle) to obtain the hand-arm mechanical impedance [4, 9].

$$Z_{\text{Hand}}(\omega) = Z_{\text{Total}}(\omega) - Z_{\text{Handle}}(\omega) \tag{1.8}$$

The impedance data can then be inverted to get the mobility of the hand-arm system and used directly in Eq. (1.7).

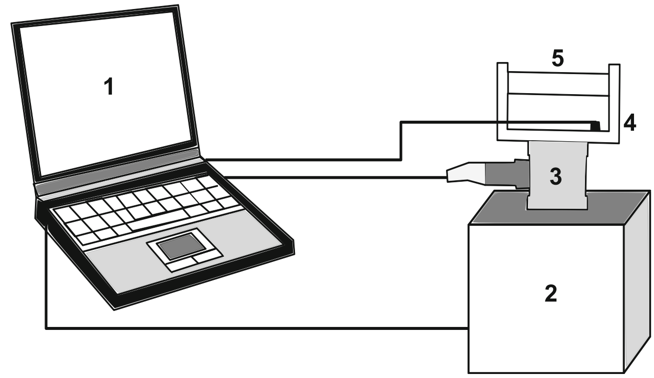

Fig. 1.3 Diagram of the hand-arm impedance measurement system (1: LMS Test.Lab 12A software, 2: Excitation device, 3: 6DOFs forces/moments sensor model MC3-A-500 from AMTI, 4: Accelerometer 356B11 type ICP from PCB Piezotronics, 5: Handle)

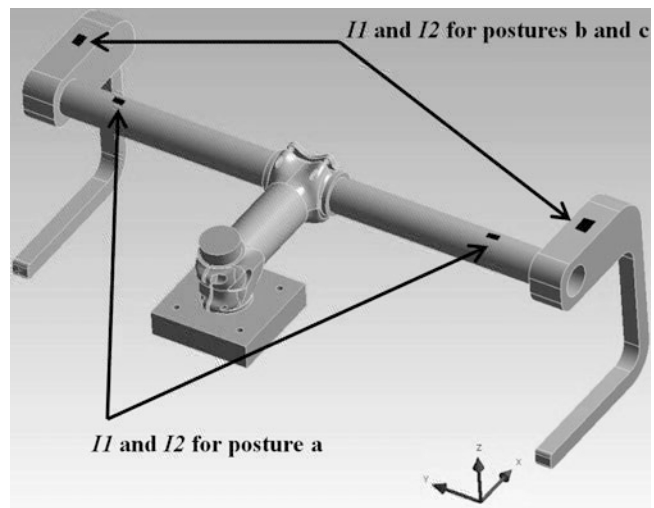

Fig. 1.4 Points location for the FE model of the assembly to obtain the needed FRFs for the different postures

The study is carried out on one subject to avoid inter-subject variability. The subject is asked to lean on the handle and to reproduce each posture to maintain the push forces along X and Z axes corresponding to the tested postures in the target measurements section. Since we are measuring each hand separately, we assume that the DC forces along X and Z axes should be half of the DC values retained when measuring on the structure assembly with both hands (target measurements).

1.2.3 Mechanical Structure Mobility

For the mechanical structure composed of a handlebar, a stem and a support, the FRFs needed for the FBS coupling process (Eq. 1.7) are obtained using an FE model (named FE FRFs). Translational DOFs (TDOFs) as well as rotational DOFs (RDOFs) are thus intrinsically available. This model of the mechanical assembly was previously updated to fit the experimental comparison in free – free conditions.

To perform the FBS coupling in Eq. (1.7), a total of 216 FE FRFs (TDOFs + RDOFs) are requested for the mechanical structure. These FRFs are obtained using the harmonic response section of the Ansys 14 Workbench software. The frequency resolution for the harmonic response of the structure is 1 Hz with a frequency span from 1 to 100 Hz. Moreover, specific commands need to be encoded to get rotational information at some points and to extract the results in *.txt files.

Considering the three different postures, the requested information in terms of FRFs are not the same for each one (Fig. 1.4)

FRFs for each posture are then computed. In Matlab, FE FRFs of the mechanical structure are coupled with experimental FRFs of both hand-arm dynamic characteristics to obtain an FBS prediction of the coupled structures.

1.3 Results

The FBS predictions for the hands coupled with the mechanical structure according to the three tested postures are compared to the target measurements corresponding to the hands holding the handlebar with the same postures and push forces. Comparisons are presented in terms of mobility along the Z-axis measured at the *I2* interface point corresponding to the right hand (Figs. 1.5, 1.6, and 1.7). In order to observe the influence of the hands touching the handlebar, the dynamic behavior of the mechanical structure alone is also shown (dotted line).

1.4 Discussion

Figures 1.5, 1.6, and 1.7 are presented with the same amplitude scale. It is possible to observe that the mobility of the structure alone at the point *I2* for posture a (Fig. 1.5) is lower than the mobility of the structure alone at the point *I2* for postures b and c (Figs. 1.6 and 1.7).

In terms of FBS prediction, the results for postures a and b (Figs. 1.5 and 1.6) demonstrate that the FBS model succeeds in providing reliable predictions for the influence of the hands on a mechanical structure with different postures and push forces applied by the subject on the structure. This is an indication that coupling between the hand-arm systems and a relatively complex mechanical structure is possible using this method.

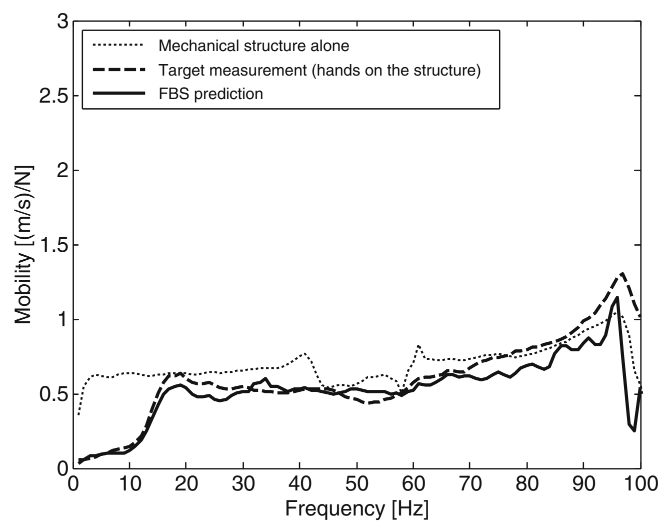

Fig. 1.5 Comparison between target measurement (hands on the structure) and FBS prediction for posture a

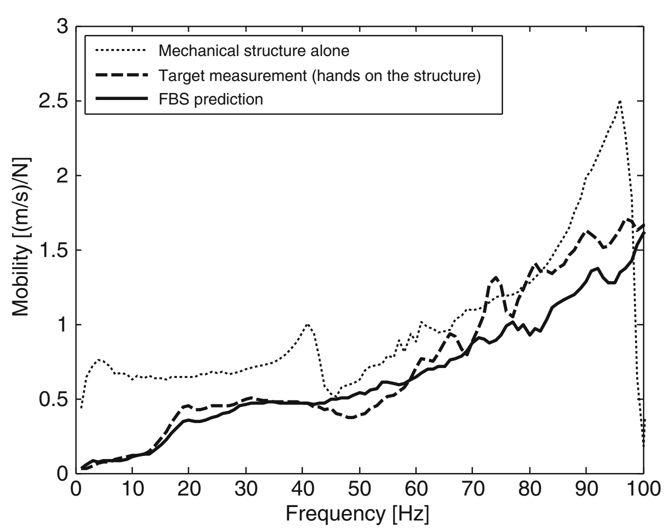

Fig. 1.6 Comparison between target measurement (hands on the structure) and FBS prediction for posture b

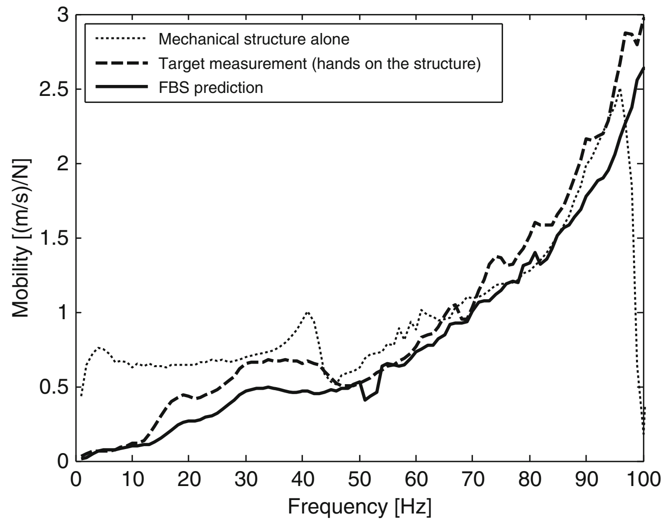

Fig. 1.7 Comparison between target measurement (hands on the structure) and FBS prediction for posture c

Nevertheless, results for posture c show some discrepancies (Fig. 1.7). The FBS model does not provide accurate results in the frequency span 1–50 Hz. This can be explained by the difficulty to reproduce the exact posture when measuring the dynamic characteristics of the hands separately. Furthermore, with such an extreme position of the wrists (see Fig. 1.2) there is an important contact surface between the hands and the mechanical structure. The hands were in contact at the two extremities of the handlebar but also with a part of the central tube while the FRFs from the FE model were obtained for a specific point. This alerts us to the fact that complex postures should be carefully reproduced during testing phases and also that the FE FRFs needed should be extracted for interface areas instead of interface points. The discrepancy between the FBS prediction and the target measurement for this specific posture may also be explained by the fact that, for hand measurement, only the vertical z-axis is considered in this work. This assumption could be too restrictive for the coupling of the hand-arm systems with the structure in this posture.

In terms of influence of the hands on the structure, we can easily identify that the posture of the subject has a clear influence on the dynamics of the assembly by looking at the target measurement of each figure from Figs. 1.5, 1.6, and 1.7. For example, with posture a, the subject provides a significant contribution to the structure dynamic up to 16 Hz while with posture b, the subject has a relatively important contribution up to 43 Hz. By integrating biodynamic measurements in the Frequency-Based Substructuring method, it is really important to control both the push force and the posture while carrying out measurements to obtain accurate predictions.

1.5 Conclusion

This study shows that reliable predictions can be obtained using the FBS method even with non-linear structures such as human body parts. Mechanical coupling predictions between the human body and a mechanical structure are thus possible using this method. Results show that it is important to control several parameters when performing the FBS coupling with a human body part because the mechanical behavior of the human body is sensitive to several factors such as position, orientation, and forces. This work also highlights the following merits of the FBS method: (1) Direct use of shaker test data, (2) Combination of substructures when only the data interfaces are known, (3) hybrid use of experimental and FE FRFs.

This work also highlights the possibility of predicting the influence of hand-arm systems on a structure using specific postures. The FBS method is a promising approach to study vibration interaction mechanisms between a mechanical structure and the human body. These results will be beneficial to further enhance interactions between humans and structures. This is a major breakthrough in human-structure interactions since it is possible to predict the influence of a human subject on a structure during the design phase of the structure in question. Limitations to this approach still remain due to the need to process a large amount of data and with regard to the computation time required for extracting FRFs.

Acknowledgements The authors gratefully acknowledge financial support from the National Science and Engineering Council of Canada (NSERC) and the participation of Cervélo and Vroomen – White Design.

References

1. Adewusi SA, Rakheja S, Marcotte P, Boileau P-E (2008) On the discrepancies in the reported human hand-arm impedance at higher frequencies. Int J Indust Ergon 38:703–714
2. Aldien Y, Marcotte P, Rakheja S, Boileau P-E (2006) Influence of hand-arm posture on biodynamic response of the human hand-arm exposed to z_h-axis vibration. Int J Ind Ergon 36:45–59
3. Aldien Y, Marcotte P, Rakheja S, Boileau P-E (2005) Mechanical impedance and absorbed power of hand-arm under x_h-axis vibration and role of hand forces and posture. Ind Health 43:495–508
4. Besa AJ, Valero FJ, Suñer JL, Carballeira J (2007) Characterization of the mechanical impedance of the human hand-arm system: the influence of vibration direction, hand-arm posture and muscle tension. Int J Ind Ergon 37:225–231
5. Burström L (1990) Measurements of the impedance of the hand and arm. Int Arch Occup Environ Health 62:431–439
6. Burström L (1997) The influence of biodynamic factors on the mechanical impedance of the hand and arm. Int Arch Occup Environ Health 69:437–446
7. Dong RG, Rakheja S, Schopper AW, Han B, Smutz WP (2001) Hand-transmitted vibration and biodynamic response of the human hand–arm: a critical review. Crit Rev Biomed Eng 29(4):391–441
8. Dong RG, Welcome DE, McDowell TW, Wu JZ (2008) Analysis of handle dynamics-induced errors in hand biodynamic measurements. J Sound Vib 318:1313–1333
9. Dong RG, Welcome DE, McDowell TW, Wu JZ (2006) Measurement of biodynamic response of human hand-arm system. J Sound Vib 294:807–827
10. Griffin MJ (1990) Handbook of human vibration. Academic, London
11. Griffin MJ, Whitham EM, Parsons KC (1982) Vibration and comfort, I. translational seat vibration. Ergonomics 25(7):603–630
12. International Standard Organization (ISO 2631) (1997) Mechanical vibration and shock—evaluation of human exposure to whole-body vibration. International Standard Organization
13. International Standard Organization (ISO/DIS 5349) (2001) Mechanical vibration—measurement and evaluation of human exposure to hand-transmitted vibration. International Standard Organization
14. Lundström R, Burström L (1989) Mechanical impedance of the human hand-arm system. Int J Ind Ergon 3:235–242
15. Marcotte P, Aldien Y, Boileau P-E, Rakheja S, Boutin J (2005) Effect of handle size and hand-handle contact force on the biodynamic response of the hand-arm system under z_h-axis vibration. J Sound Vib 283:1071–1091
16. Mansfield NJ (2005) Human response to vibration. CRC
17. Reynolds DD, Angevine EN (1977) Hand-arm vibration, Part II: vibration transmission characteristics of the hand and arm. J Sound Vib 51(2):255–265
18. Richard S (2005) Étude du comportement dynamique d'un vélo de route en lien avec le confort du cycliste. MScA Thesis, Université de Sherbrooke
19. Richard S, Champoux Y (2006) Development of a metric related to the dynamic comfort of a road bike. In: Proceedings of the IMAC XXIV, St. Louis, 2006
20. Avitabile P (2003) Twenty years of structural dynamic modification: a review. Sound Vib 14–25
21. Craig R, Bampton M (1968) Coupling of substructures for dynamic analysis. AIAA J 6(7):1313–1319
22. De Klerk D, Rixen D, De Jong J (2006) Frequency based substructuring (FBS) method reformulated according to the dual domain decomposition method. In: Proceedings of the fifteenth international modal analysis conference, Society for Experimental Mechanics, Paper 136, 2006
23. De Klerk D, Rixen DJ, Voormeeren SN, (2008) General framework for dynamic substructuring—history, review, and classification of techniques. AIAA J 46(5)
24. Ewins DJ (2000) Modal testing: theory, practice and application, 2nd edn. Research Studies Press
25. Hurty WC (1960) Vibrations of structural systems by component mode synthesis. J Eng Mech/Am Soc Civil Eng 86(4):51–69
26. Jetmundsen B (1986) On frequency domain methodologies for prescribed structural modification and subsystem synthesis. PhD Thesis, Rensselaer Polytechnic Institute, New York
27. Jetmundsen B, Bielawa R, Flanelly W (1988) Generalized frequency domain substructure synthesis. J Am Helicop Soc 33(1):55–65
28. Klosterman A (1971) On the experimental determination and use of modal representations of dynamic characteristics. Ph.D. Thesis, University of Cincinnati, Department of Mechanical Engineering
29. MacNeal R (1971) Hybrid method of component mode synthesis. Comput Struct 1(4):581–601
30. Mayes RL (2012) Tutorial on experimental dynamic substructuring using the transmission simulator method. In: Proceedings of the 30th international modal analysis conference. Society for experimental mechanics (Topics in experimental dynamics substructuring and wind turbine dynamics), pp 1–9
31. Perrier SS, Champoux Y, Drouet J-M (2012) Using substructuring to predict the human hand influence on a mechanical structure. In: Proceedings of the 30th international modal analysis conference. Society for Experimental Mechanics (Topics in experimental dynamics substructuring and wind turbine dynamics), pp 33–44
32. Lépine J, Champoux Y, Drouet J-M (2011) Excitation techniques for testing bike vibration transmission in the laboratory. In: Proceedings of the 29th International modal analysis conference. Society for experimental mechanics (Sensors, Instrumentation and Special Topics), p 35

Chapter 2
Investigation of Modal Iwan Models for Structures with Bolted Joints

Brandon J. Deaner, Matthew S. Allen, Michael J. Starr, and Daniel J. Segalman

Abstract Structures with mechanical joints are difficult to accurately model; even when the natural frequencies of the system remain essentially constant, the damping introduced by the joints is often observed to depend nonlinearly on amplitude. Although models for individual joints have been employed with some success, the modeling of a structure with many joints remains a significant obstacle. This work explores whether nonlinear damping can be applied in a modal framework, where instead of modeling each discrete joint within a structure, a nonlinear damping model is used for each mode of interest. This approach assumes that the mode shapes of the structure do not change significantly with amplitude and that there is negligible coupling between modes. The nonlinear Iwan joint model has had success in modeling the nonlinear damping of individual joints and is used as a modal damping model in this work. The proposed methodology is first evaluated by simulating a structure with a small number of discrete Iwan joints (bolted joints) in a finite element code. A modal Iwan model is fit to simulated measurements from this structure and the accuracy of the modal model is assessed. The methodology is then applied to actual experimental hardware with a similar configuration and a modal damping model is identified for the first few modes of the system. The proposed approach seems to capture the response of the system quite well in both cases, especially at low force levels when macro-slip does not occur.

Keywords Nonlinear damping • Bolted joints • Iwan model • Energy dissipation • Modal damping

2.1 Introduction

Mechanical joints are known to be a major source of damping in jointed structures. However, the physics at the interface are quite complex and the amplitude dependence of damping in mechanical joints has proven quite difficult to predict. For many systems, linear damping models seem to capture the response of a structure at calibrated force levels. However, that approach relies on testing the structure at large force levels to calibrate the model. Furthermore, that approach can be over conservative or even erroneous since a linear model does not capture the amplitude dependence of the damping. Thus, it is crucial to understand how mechanical joints behave at a range of force levels so that the response of a jointed structure can be modeled accurately.

In this work, nonlinearities associated with mechanical joints will be classified into two different regions, micro-slip and macro-slip. Consider the joint shown in Fig. 2.1, where a bolt is used to connect two slabs of material. The preload in the bolt creates a contact region between the two slabs near the bolt. If a force F is applied to the slabs, slip will occur at the

B.J. Deaner (✉) • M.S. Allen
Department of Engineering Physics, University of Wisconsin-Madison, 534 Engineering Research Building, 1500 Engineering Drive, Madison, WI 53706, USA
e-mail: bdeaner@wisc.edu; msallen@engr.wisc.edu

M.J. Starr
Component Science and Mechanics, Sandia National Laboratories, P.O. Box 5800, Albuquerque, New Mexico, 87185, USA
e-mail: mjstarr@sandia.gov

D.J. Segalman
Component Science and Mechanics, Sandia National Laboratories, P.O. Box 969, Mail Stop 9042, Livermore, California, 94551, USA
e-mail: djsegal@sandia.gov

R. Mayes et al. (eds.), *Topics in Experimental Dynamic Substructuring, Volume 2: Proceedings of the 31st IMAC, A Conference on Structural Dynamics, 2013*, Conference Proceedings of the Society for Experimental Mechanics Series 36,
DOI 10.1007/978-1-4614-6540-9_2, © The Society for Experimental Mechanics, Inc. 2014

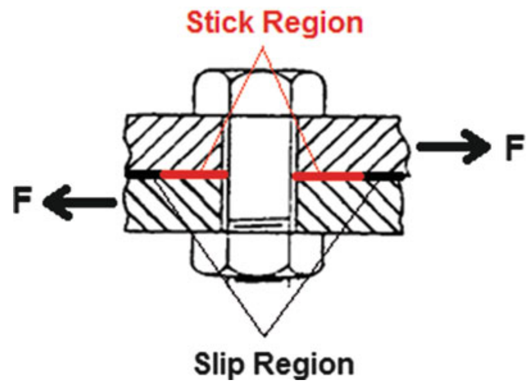

Fig. 2.1 Contact and Slip regions are shown for a mechanical joint undergoing micro-slip [1]

outskirts of the contact region. This means that there will be a region of stick and a region of slip as indicated in Fig. 2.1. For this case, the bolted joint is said to be undergoing micro-slip due to the small slip displacements that cause the frictional energy loss [1].

Macro-slip occurs when the stick region vanishes and larger slip displacements are possible. If a very large displacement is considered, the slabs of material will eventually come into contact with the bolt. This further complicates the system and is not considered in this work.

To capture the response of the joint in both the micro-slip and macro-slip regions, a 4-Parameter Iwan model was developed in [2]. This constitutive model has a small number of parameters and yet accounts for the key characteristics of the joint's response including the joint slip force (F_S), joint stiffness (K_T), and power law energy dissipation (χ, β). In the past decade, the 4-Parameter Iwan model has been implemented to predict the vibration of structures with a few discrete joints [3, 4]. However, when modeling individual joints, each joint requires a unique set of parameters $\{F_S, K_T, \chi, \beta\}$, which means that hundreds or even thousands of joint parameters may need to be deduced for the systems of interest. On the other hand, when a small number of modes are active in a response, some measurements have suggested that a simpler model may be adequate. Segalman investigated the idea of applying the 4-Parameter Iwan model in a modal framework in [5]. He used simulated measurements to deduce the modal Iwan parameters for two simple spring mass systems and compared this to the more rigorous approach where each discrete joint in the system was treated separately.

This work builds on Segalman's work [5] by simulating a more realistic finite element structure. First, a structure with four discrete Iwan joints is modeled using finite elements and the simulated response data is used to deduce a set of modal Iwan parameters. Particular attention is given to the degree to which the modal Iwan model captures the response of the finite element model that includes discrete Iwan joints. The methodology is then applied experimentally to an actual beam with a small link attached through two bolted joints. The beam was tested with free-free conditions, and great care had to be taken to assure that the suspension system did not dominate the measured damping. The initial results are promising, revealing that the modal Iwan approach does capture the response of the actual structure quite well in the micro-slip regime.

2.2 Nonlinear Energy Dissipation Model

The 4-Parameter Iwan model that is used in this work was initially presented in [2]. A historical review of the major contributors prior to Iwan's work led to the Iwan model being referred to as the Bauschinger-Prandtl-Ishlinskii-Iwan (BPII) model in a more recent work [6]. However, for simplicity and consistency with previous works, in this work the constitutive model will be referred to as the Iwan model.

2.2.1 Parallel–Series Iwan Model

A parallel arrangement of elements, each composed of a spring and frictional damper in series, is referred to as a parallel–series model in [7]. The physical representation of a parallel–series Iwan model is shown in [2]. The force in the joint, $F(t)$, is shown to have the following form,

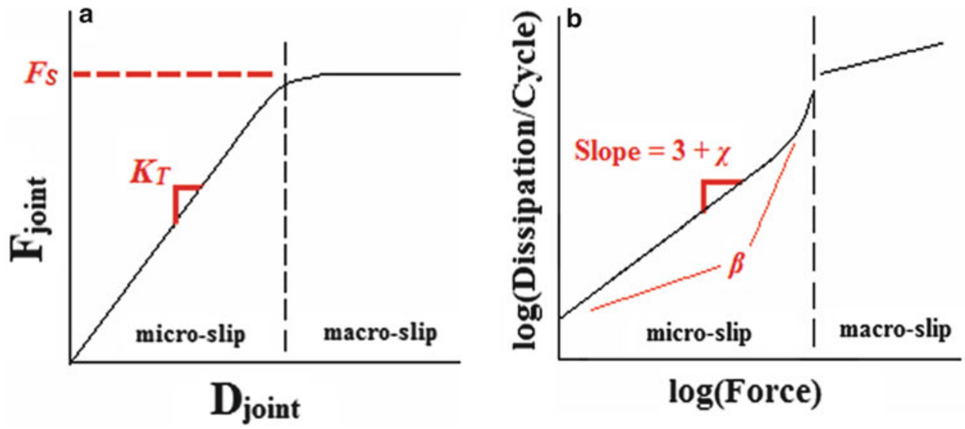

Fig. 2.2 (**a**) Both macro-slip force (F_S) and joint stiffness (K_T) can be found from the force-displacement relationship of the joint. (**b**) The χ value is found from the slope of the dissipation and the β value is a measure of dissipation level and shape of the dissipation curve

$$F(t) = \int_0^\infty \rho(\phi)\,[u(t) - x(t,\phi)]\,d\phi \tag{2.1}$$

where

$$\dot{x}(t,\phi) = \begin{cases} \dot{u} & \text{if } \|u - x(t,\phi)\| = \phi \text{ and } \dot{u}\,[u - x(t,\phi)] > 0 \\ 0 & \text{otherwise} \end{cases} \tag{2.2}$$

and $u(t)$ is the extension of the joint, $x(t,\phi)$ is the displacement of the frictional damper with strength ϕ and $\rho(\phi)$ is the population density of the spring and frictional damper elements with strength ϕ.

The responseproperties of the Iwan joint are characterized by the population density $\rho(\phi)$. Various population densities and their limitations are discussed in [6, 8]. Experiments at small force levels have revealed that the energy dissipated by the joint over one vibration cycle tends to be a power of the applied force. Analytically, the energy dissipation associated with pure material damping yields a power of 2.0, while the energy dissipation associated with friction between two bodies when the contact pressure is uniform yields a power of 3.0 [1, 2, 9, 10]. Experimentally, the dissipation tends to have a power-law slope that ranges between 2.0 and 3.0 [10]. One explanation for why experimental results often dissipate energy at a power less than 3.0 is due to the presumption that the contact pressure is nonuniformly distributed in joints [9].

In any event this means that at small force levels, a population density that dissipates energy in a power-law type fashion is desired. At large force levels, joints are known to exhibit a discontinuous nonlinearity associated with the initiation of macro-slip. This characteristic of joints must also be accounted for by the population density.

2.2.2 4-Parameter Iwan Model

To accommodate the behavior of joints at a large range of forces, a 4-parameter population density was developed in [2] with the form:

$$\rho(\phi) = R\phi^{\chi}\,[H(\phi) - H(\phi - \phi_{\max})] + S\delta(\phi - \phi_{\max}) \tag{2.3}$$

where $H(\,)$ is the Heaviside step function, $\delta(\,)$ is the Dirac delta function and the four parameters that characterize the joint include: R, which is associated with the level of energy dissipation, χ, which is directly related to the power law behavior of energy dissipation, $\phi_{\max}$, which is equal to the displacement at macro-slip, and the coefficient S, which accounts for a potential discontinuous slope of the force displacement plot when macro-slip occurs.

The four parameters $\{R, \chi, \phi_{\max}, S\}$ are converted to more physically meaningful variables $\{K_T, F_S, \chi, \beta\}$ in [2, 4]. F_S is the joint force necessary to initiate macro-slip, K_T is the stiffness of the joint, χ is directly related to the slope of the energy dissipation in the micro-slip regime, and β relates to the level of energy dissipation and the shape of the energy dissipation curve as the macro-slip force is approached.

This new set of parameters, $\{K_T, F_S, \chi, \beta\}$, can be deduced from the two plots seen in Fig. 2.2. Given a set of simulation or experimental data, there are a variety of methods that could be used to find the energy dissipation and joint force. A few of

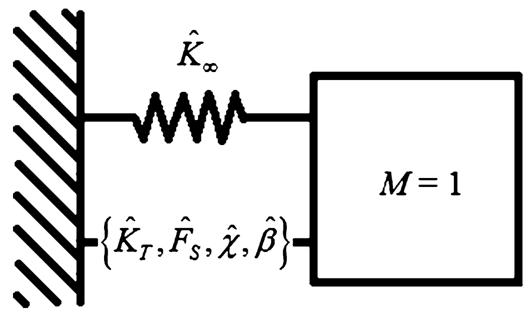

Fig. 2.3 Schematic of the model for each modal degree of freedom. Each mode has a unique set of Iwan parameters that characterize its nonlinear damping (and to a lesser extent stiffness)

these methods will be highlighted in Sect. 2.2.4. Once these are known, the Iwan parameters can be determined graphically, or using nonlinear optimization as discussed in [2], or through some combination of the two. This work focuses on the graphical approach as it lends more insight into the importance of each parameter and its validity.

If we consider a system where the damping is strictly due to the 4-Parameter Iwan model, the governing equation becomes

$$M\ddot{x} + K_\infty x = F^X + F^J \tag{2.4}$$

where M and K_∞ are the linear mass and stiffness matrices of a finite element model, F^X is the vector of external forces, and F^J is a vector of nonlinear joint forces that the joint applies to the structure. Note that F^J is the 4-parameter Iwan model defined in Eq. (2.1) with opposite sign convention. F^J has nonzero entries corresponding to the two ends where the joint is attached to the finite element model and depends on the displacement at those points.

As discussed previously, the 4-parameter Iwan model has been implemented to predict the response of structures with a small number of discrete joints [3, 4]. However, each joint requires a unique set of parameters $\{K_T, F_S, \chi, \beta\}$, so many joint parameters need to be deduced and it is not likely that they can all be determined uniquely from a set of experimental measurements.

2.2.3 Modal Iwan Model

In order to circumvent this limitation, Segalman proposed that energy dissipation be applied on a mode-by-mode basis, using the 4-parameter Iwan constitutive model [5]. The Iwan model is assumed to be applicable to each mode, although the parameters of each mode are tuned to match experimental measurements and hence aren't necessarily the same as the parameters of any individual joint in the structure. In general, the nonlinearity that joints introduce can couple the modes of a system so that modes in the traditional linear sense can not be defined. However, experiments have often shown that structures with joints are typically quite linear, suggesting that one might be able to model the structure as a collection of uncoupled linear modes, each with nonlinear damping characteristics. This would allow one to model a structure with a relatively small number of modes that capture its performance in the frequency band of interest, and the response of each mode could be found through a nonlinear, single degree-of-freedom simulation. Specifically, each modal degree-of-freedom is modeled by a single degree-of-freedom oscillator, as shown in Fig. 2.3, with a 4-parameter Iwan model placed between the modal degree of freedom and the ground. A second spring is placed in parallel with the 4-parameter Iwan model, representing the residual stiffness of that mode when the Iwan model is in macro-slip.

Again, the modal Iwan parameters $\left\{\hat{K}_T, \hat{F}_S, \hat{\chi}, \hat{\beta}\right\}$ in Fig. 2.3 will not be the same as the $\{K_T, F_S, \chi, \beta\}$ parameters of any discrete Iwan joint parameters in the structure.

The response for each mode r is then governed by the following differential equation,

$$\ddot{q}_r + \omega_{0,r}^2 q_r = \Phi_r{}^{\mathrm{T}} F^X + \hat{F}_{J,r} + \hat{K}_{T,r} q_r \tag{2.5}$$

where ϕ_r and ω_0 are found by solving the eigenvalue problem $\left[[K_0] - \omega_{0,r}^2\right]\Phi_r = 0$ and $\hat{F}_{J,r}$ is the modal joint force and $\hat{K}_{T,r}$ is the modal joint stiffness for the r^{th} mode. The low force mode shapes are used to define the modal parameters, so the stiffness matrix used in the eigenvalue problem above must include the low-force stiffness of the joints, i.e. $[K_0] = [K_\infty] + [K_T]$, where $[K_T]$ is a matrix that captures the stiffness that the joints contribute to the structure when the load is infinitesimal. This presumes that the stiffness of the joints has been included when calculating the mode shapes ϕ_r and natural frequencies ω_0 of the structure (i.e. the modal Iwan model exhibits no slip). In practice, these modal parameters will come from a low-level modal test and so this assumption should be valid. On the other hand, if the structure is modeled in finite elements then the stiffness of the joints should be included when calculating the mode shapes; this functionality is built into the Sierra/SD (Salinas) finite element package [11, 12].

2.2.4 Extracting Frequency and Energy Dissipation Data

In this work, the modal Iwan parameters $\left\{\hat{K}_T, \hat{F}_S, \hat{\chi}, \hat{\beta}\right\}$ will be extracted by estimating the frequency and energy dissipation from the free response of each mode of interest. Two methods for calculating frequency and energy dissipation were explored in this work.

2.2.4.1 Peak-Picking and Zero-Crossing Approach

The first method was developed by Segalman in an unpublished document. The time history of the acceleration is approximated as

$$a(t) = e^{P(t)} \cos\left(\omega(t)t\right) \tag{2.6}$$

where $e^{P(t)}$ is the envelope of the response, and $\omega(t)$ is the instantaneous frequency. The envelope $e^{P(t)}$ is found by identifying the acceleration peaks and fitting a cubic spline to the logarithm of those peaks. The frequency $\omega(t)$ is found by calculating the zero-crossings of a response. The energy dissipation per cycle is calculated using the change in peak kinetic energy and is given by

$$KE_P = \frac{M}{2} v_P^2 = \frac{M}{2} \frac{e^{2P(t)}}{\omega^2} \tag{2.7}$$

where v_P is the peak velocity of each cycle. The change in peak kinetic energy is calculated by taking the derivative of the peak kinetic energy which is then multiplied by the period ($2\pi/\omega$) to estimate the energy dissipation per cycle D. This assumes that kinetic energy changes slowly relative to the period so that it can be approximated as constant over each cycle.

$$D \approx \frac{dKE_P}{dt} \frac{2\pi}{\omega} = \frac{4\pi}{\omega} \frac{dP(t)}{dt} KE_P \tag{2.8}$$

2.2.4.2 Hilbert Transform with Polynomial Smoothing Approach

The second method uses the Hilbert transform along with curve fitting to smooth the instantaneous phase and amplitude found from a Hilbert transform [13, 14]. An analytic signal is formed when the Hilbert transform, $\tilde{a}(t)$, is added to the acceleration response [15]

$$A(t) = a(t) + i\tilde{a}(t) \tag{2.9}$$

The magnitude of the analytic signal is the envelope of the response and is approximated by

$$Z(t) = |A(t)| = A_0 \exp\left(-\zeta(t)\omega_n(t)\right) \tag{2.10}$$

where A_0 is the initial amplitude, $\omega_n(t)$ is the frequency, and $\zeta(t)$ is the coefficient of critical damping. The instantaneous phase is obtained from the analytic signal using the following equation.

$$\varphi(t) = \tan^{-1}\left(\frac{\tilde{a}(t)}{a(t)}\right) \tag{2.11}$$

In other works, for example those by Feldman [15], the instantaneous natural frequency is apparently found by low-pass filtering and then differentiating the phase. However, those works give little detail regarding the optimal low-pass filter and

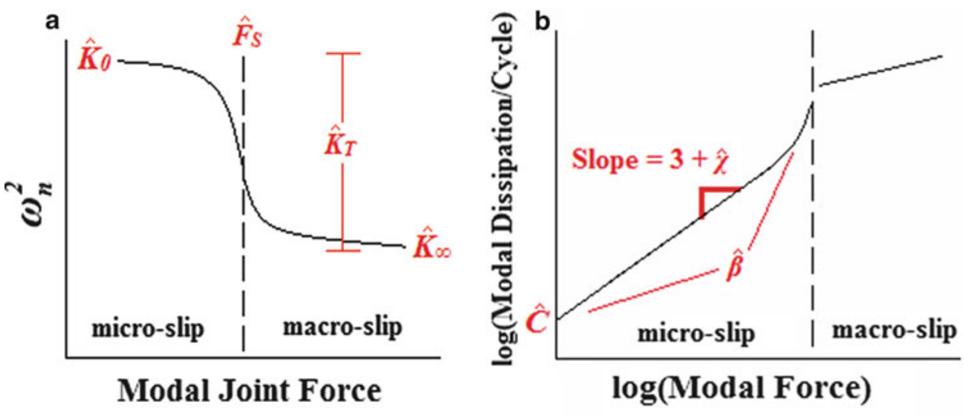

Fig. 2.4 (**a**) Modal macro-slip force ($\hat{F}_S$) and modal joint stiffness ($\hat{K}_T$) can be found from the softening seen in the natural frequency. (**b**) The $\hat{\chi}$ value is found from the slope of the modal dissipation and the $\hat{\beta}$ value is a measure of modal dissipation level and shape of the modal dissipation curve

the results depend heavily on the filter used. If the response is not filtered then noise in the measured response is amplified by the differentiation making the results meaningless, even when the noise is quite small (e.g. integration error in the simulations presented here). In this work, the measured phase is smoothed by fitting a polynomial to the data before differentiating [13]. In addition, the beginning and end of the phase data are deleted since they tend to be contaminated by end effects in the Hilbert Transform.

Both methods for extracting the frequency and energy dissipation data were explored in this work. In general, the Hilbert Transform with Curve Fitting approach was found to smooth out the data more effectively than the peak-picking/zero-crossing approach and will be used in the plots shown in this paper.

2.2.5 Deducing Modal Iwan Parameters

This section explains how modal Iwan parameters are deduced from energy dissipation versus force measurements. The procedure closely follows that used by Segalman in [5] and the work done by Guthrie, which was described in an unpublished memo. The methods described in the previous section provide a set of frequency and energy dissipation data such as that shown schematically in Fig. 2.4. Note that these are quite similar to those shown in Fig. 2.2 for a discrete joint, except that all of the quantities, such as the slip force, are now in a modal form rather than physical. Also, since the modal Iwan model has a linear spring in parallel, its stiffness does not go to zero at macro-slip but instead it simply drops to K_∞.

The $\hat{\chi}$ parameter is found by fitting a line to the data for the log of energy dissipation versus log of the modal force at low force levels. Then the $\hat{\chi}$ parameter for each mode r is given by the slope of that line minus three:

$$\hat{\chi}_r = \text{Slope}_r - 3 \tag{2.12}$$

In order to deduce the Iwan modal stiffness $\hat{K}_T$, the natural frequencies of each mode are plotted versus modal joint force. A softening of the system, characterized by a drop in frequency, illustrates the amount of modal stiffness associated with all the relevant joints of the system. Assuming that the mode shapes used in the modal filtering process are mass normalized, the equation for modal joint stiffness for each mode becomes

$$\hat{K}_{T,r} = \hat{K}_{0,r} - \hat{K}_{\infty,r} = \omega_{0,r}^2 - \omega_{\infty,r}^2 \tag{2.13}$$

where ω_0 is the natural frequency corresponding to the case when all the joints in the structure exhibit no slipping, and ω_∞ is the natural frequency when all of the joints are slipping. This points to the major advantage of using a modal Iwan implementation as opposed to a discrete Iwan implementation. For a modal Iwan implementation, only the modal stiffness and modal slip force of each kept mode needs to be considered as opposed to calculating the stiffness and slip force associated with each joint individually.

The modal joint slip force, $\hat{F}_S$, can be estimated from Fig. 2.4. To find the last parameter, $\hat{\beta}$, all of the previous parameters found are needed along with the y-intercept, $\hat{C}$, of the line that was fit in order to find the $\hat{\chi}$ parameter. Then, the following equation was formed from [2] that can be used to solve for $\hat{\beta}$ numerically.

$$\hat{F}_{s,r} = \left[\frac{4\left(\hat{\chi}_r + 1\right) \hat{K}_{T,r}^{\chi_r+2} \left(\hat{\beta}_r + \frac{\hat{\chi}_r+1}{\hat{\chi}_r+2}\right)^{\hat{\chi}_r+1}}{\hat{C}_r K_{\infty,r}^{(3+\hat{\chi}_r)} \left(2 + \hat{\chi}_r\right)\left(3 + \hat{\chi}_r\right)\left(1 + \hat{\beta}_r\right)^{\hat{\chi}_r+2}} \right]^{\frac{1}{\hat{\chi}_r+1}} \tag{2.14}$$

Once all of these parameters have been determined, one can reconstruct the modal energy dissipation versus force curve for the modal Iwan model and compare it to the measurements. This is helpful, since experience has revealed that it is sometimes necessary to adjust the parameters $\{\hat{K}_T, \hat{F}_S, \hat{\beta}\}$ so that the dissipation versus force curve accurately fits the measurements. In the micro-slip region, the modal energy dissipation per cycle, $\hat{D}_r$, is adapted from [2] and is given by,

$$\hat{D}_r = 4\hat{r}_r^{\hat{\chi}_r+3} \left(\frac{\hat{F}_{S,r}}{\hat{K}_{T,r}}\right) \left(\frac{(\hat{\beta}_r + 1)(\hat{\chi}_r + 1)}{\left(\hat{\beta}_r + \frac{\hat{\chi}_r+1}{\hat{\chi}_r+2}\right)^2 \left(\hat{\chi}_r + 2\right)\left(\hat{\chi}_r + 3\right)}\right) \tag{2.15}$$

where $\hat{r}_r$ is found by iteratively solving:

$$\frac{\hat{F}_{J,r}}{\hat{F}_{S,r}} = \hat{r}_r \left(\frac{(\hat{\beta}_r + 1) - \frac{\hat{r}_r^{\hat{\chi}_r+1}}{\hat{\chi}_r+2}}{\hat{\beta}_r + \frac{\hat{\chi}_r+1}{\hat{\chi}_r+2}}\right) \tag{2.16}$$

For the macro-slip region, modal energy dissipation is given by:

$$\hat{D}_r = 4q_{p,r}\hat{F}_{S,r} \tag{2.17}$$

where $q_{p,r}$ is the peak modal displacement over a cycle of the response.

2.3 Finite Element Simulations

Both the discrete 4-parameter Iwan model and the modal Iwan model have been implemented into Sierra/SD (Salinas), a structural dynamics finite element code developed by Sandia National Laboratories [11, 12]. Sierra/SD was used to simulate the response of a structure with several discrete Iwan joints, in order to generate response data that was then fit to a modal Iwan model. Then the response of the modal Iwan model could be compared to that of the truth model to evaluate the proposed procedure.

2.3.1 Finite Element Model

The model of interest is a beam with a link attached to the center of the beam. The general dimensions of the beam ($20'' \times 2'' \times 0.25''$) and link ($3.5'' \times 0.5'' \times 0.125''$) are shown in Fig. 2.5. The beam is meshed with fairly course hexahedron elements (approximate edge length varies between $0.125''$ and $0.25''$) with a total of 1,554 nodes to keep the computational cost reasonable. The first five natural frequencies of this model were compared to the natural frequencies of a finely meshed model containing 37,553 nodes, and it was found that the error was less than 1%.

The representative model has four square washers in contact with the beam as seen in Fig. 2.6. Four Iwan elements are defined for the two in-plane shear directions at the contact patches between the washers and the beam. Note that no other damping is included in this model, so for the discrete Iwan simulations, all of the energy dissipation is due to the Iwan model.

In addition to the Iwan elements defined in the in-plane directions, constraints are placed on all out-of-plane rotations and displacements to prevent penetration and separation between the washers and the beam. Two of the washers are merged to the link which adds stiffness to the beam. The beam, link, and washers are given the linear elastic material properties of Stainless Steel 304.

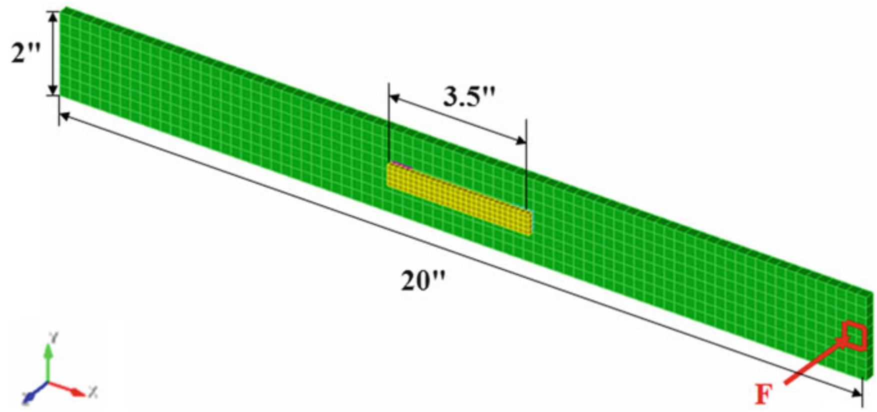

Fig. 2.5 Computational model of a beam with several discrete Iwan joints

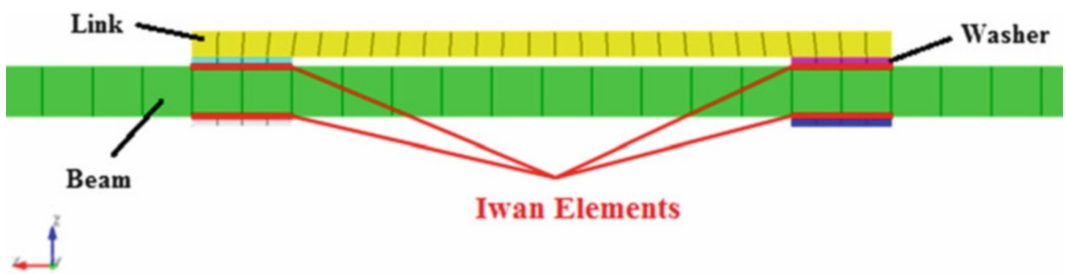

Fig. 2.6 Location of discrete Iwan joints. An Iwan joint is used at each surface where the washers come into contact with the beam

Table 2.1 Iwan parameters used for the discrete Iwan simulations

K_T (lb/in)	F_S (lb)	χ	β
$2.75{\cdot}10^5$	300	−0.3	0.02

2.3.2 Discrete Iwan Simulations

An experiment was simulated by exciting the finite element model with an impulsive force. The force was applied to nine nodes at the tip of the beam as shown in Fig. 2.5. A haversine forcing function was used with a duration of 1.6 ms. The duration of the force was chosen to primarily excite the first three elastic modes of vibration which will be analyzed in this work.

The acceleration time histories at all nodes were extracted and filtered using the pseudo inverse of the mode shape matrix including the first 50 mode shapes from a linear eigenanalysis. This was accomplished using a modal filter [16], i.e. by approximating the response as follows,

$$\ddot{x} = \Phi \ddot{q} \tag{2.18}$$

where ϕ is the mode shape matrix including the first 50 linear modes, and then pre-multiplying both sides of Eq. (2.18) with the pseudo-inverse of the mode shape matrix.

The discrete Iwan parameters used for these simulations were those found from previous experimental studies of a lap joint [2]. The parameters for all four discrete Iwan elements are shown in Table 2.1.

2.3.3 Modal Iwan Simulations

The methodology described in Sect. 2.2.5 was then used to deduce the modal Iwan parameters of the first three elastic bending modes. The modal Iwan model was then used to predict the response of the system to the impulsive force used for the discrete Iwan simulations. This was done using the implementation of the modal Iwan model in the Sierra/SD finite element code. Hence, it was fairly straightforward to obtain the response of the modal model at every node of the finite element model. The modal coordinate amplitudes were not provided directly, so they were estimated from the acceleration time histories using

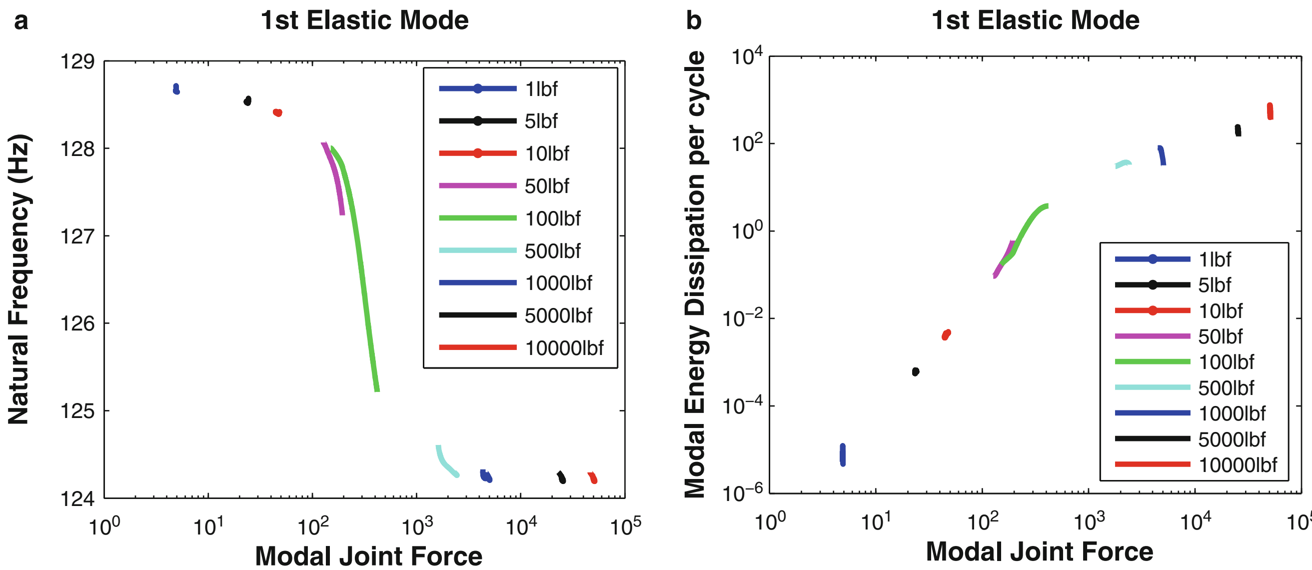

Fig. 2.7 Natural frequency (**a**) and energy dissipation (**b**) versus modal joint force for the 1st elastic mode of the finite element model. The change in the natural frequency observed in (**a**) is used to find the modal joint stiffness ($\hat{K}_T$) and the sharp change in slope in (**b**) is used to find the modal macro-slip force ($\hat{F}_S$)

Table 2.2 Iwan parameters used for the discrete Iwan simulations

Mode	$\hat{K}_T$	$\hat{F}_S$	$\hat{\chi}$	$\hat{\beta}$
1st Elastic	$4.45 \cdot 10^4$	239.4	−0.183	0.3
2nd Elastic	$2.0 \cdot 10^4$	$1.0 \cdot 10^5$	−0.999	3.0
3rd Elastic	$8.73 \cdot 10^5$	534.6	−0.048	0.38

the same process described previously. Both simulations were integrated using a Newmark-Beta integration scheme with an iterative Newton loop to solve the residual force equation. The step size was set to $1 \cdot 10^{-5}$ seconds with 20,000 time steps for a total time history of 0.2 seconds.

2.3.4 Simulation Results

The response of the truth model (i.e. that in Sect. 2.3.2) was modally filtered and the modal energy dissipation versus force was found using the procedure described in Sect. 2.2.4. The modal joint stiffness $\hat{K}_T$ and modal macro-slip force $\hat{F}_S$ were then estimated from this data, shown in Fig. 2.7. Figure 2.7 shows the frequency versus modal joint force, $\hat{F}_J$ in Eq. (2.5), was estimated from the simulated measurements. Figure 2.7 shows the modal energy dissipation, $\hat{D}$ in Eq. (2.8), versus modal joint force. Notice that the joint transitions to macro-slip over a range of forces so the modal slip force cannot be determined precisely. The modal Iwan parameters were deduced using the procedure described in Sect. 2.2.5, and the parameters obtained are shown in Table 2.2 for the first three elastic bending modes.

2.3.4.1 Comparison of Modal Time Responses

Now that the modal model has been identified, one can compare its response to that of the finite element truth model in Sect. 2.3.2. To simplify the comparison, the modal responses of the first mode were first assessed with impact force levels of 10 lbf and 1000 lbf, and the comparison is shown in Fig. 2.8. The modal responses agree very precisely at the 10lbf level. On the other hand, when an impact force with an amplitude of 1000lbf is applied to the model, the modal Iwan model seems to damp the response more than the discrete Iwan model. It is also interesting to note the sharp initial increase in modal acceleration due to the impact force, which seems to be well captured at both force levels.

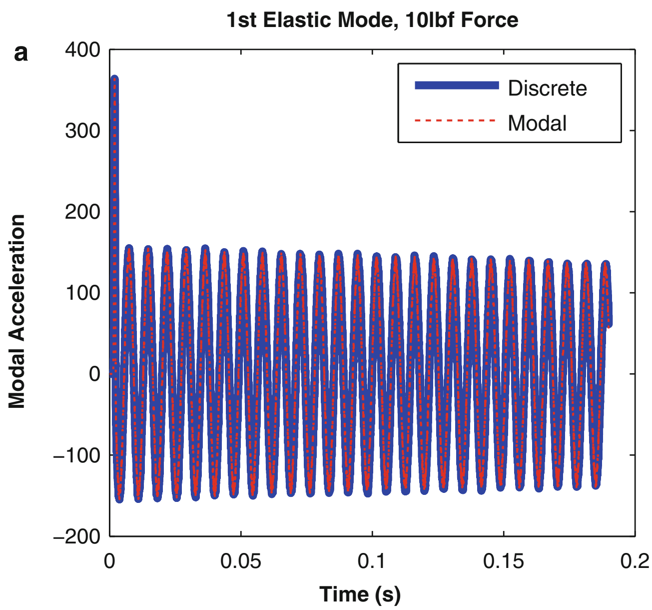

Fig. 2.8 Comparison of the response of the first elastic mode for both the Modal and Discrete Iwan models for impact forces of 10 lbf (**a**) and 1000 lbf (**b**)

Fig. 2.9 Modal energy dissipation versus modal force for the 1st elastic mode. The *colored lines* show simulations of the finite element truth model (with discrete Iwan joints) and the *black dashed line* shows the dissipation for the modal Iwan model. The two compare well for a range of impact forces from 1 lbf to 10,000 lbf (color figure online)

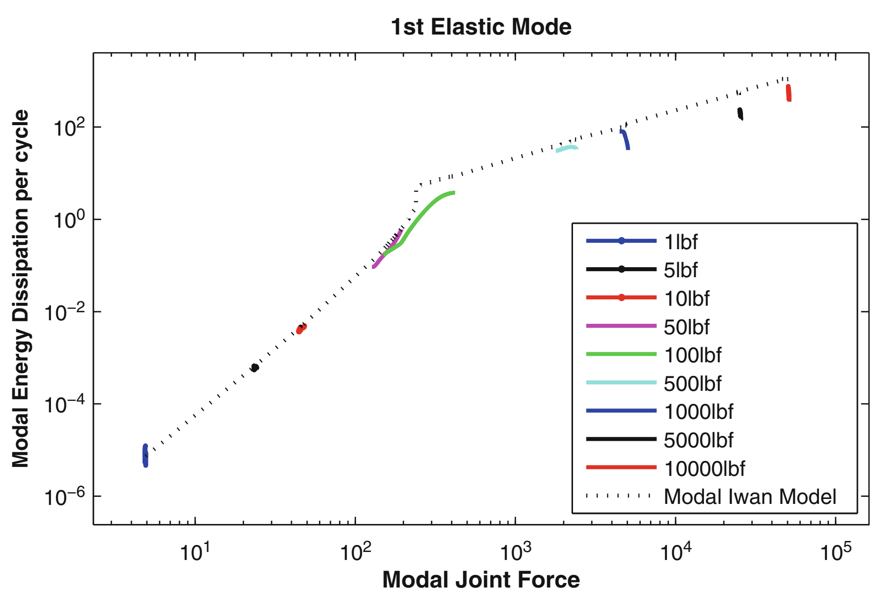

It becomes clear that one would have to compare a large number of time histories to assess the performance of the modal Iwan model over the force range of interest. It is more effective to compare the modal energy dissipation that each model gives over the entire range of modal force. The energy dissipation of the modal Iwan model was computed using Eq. (2.15), (2.16), and (2.17) and compared to that used to construct the model, as shown in Fig. 2.9.

2.3.4.2 Comparison of Modal Energy Dissipation

The comparison for the 1st elastic mode, in Fig. 2.9, reveals that the modal Iwan model does a very good job of predicting the energy dissipation for a range of impact loads that span the micro-slip and macro-slip regions. However, the data at higher force levels shows considerable scatter and the agreement is not as good at those force levels. This is why the comparison in Fig. 2.8 showed the modal Iwan model over-predicting the damping in the system at high force levels. Based on Fig. 2.9, one would expect a similar level of disagreement at 5,000 and 10,000 lbf.

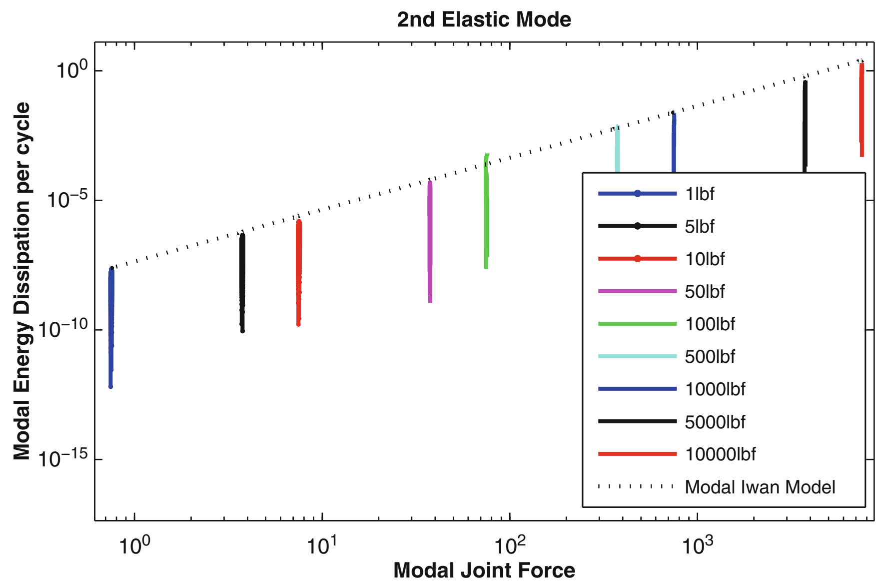

Fig. 2.10 Modal energy dissipation versus modal force for the 2nd elastic mode. The 2nd bending mode is lightly damped and the fit reveals that this mode can be well approximated as linear

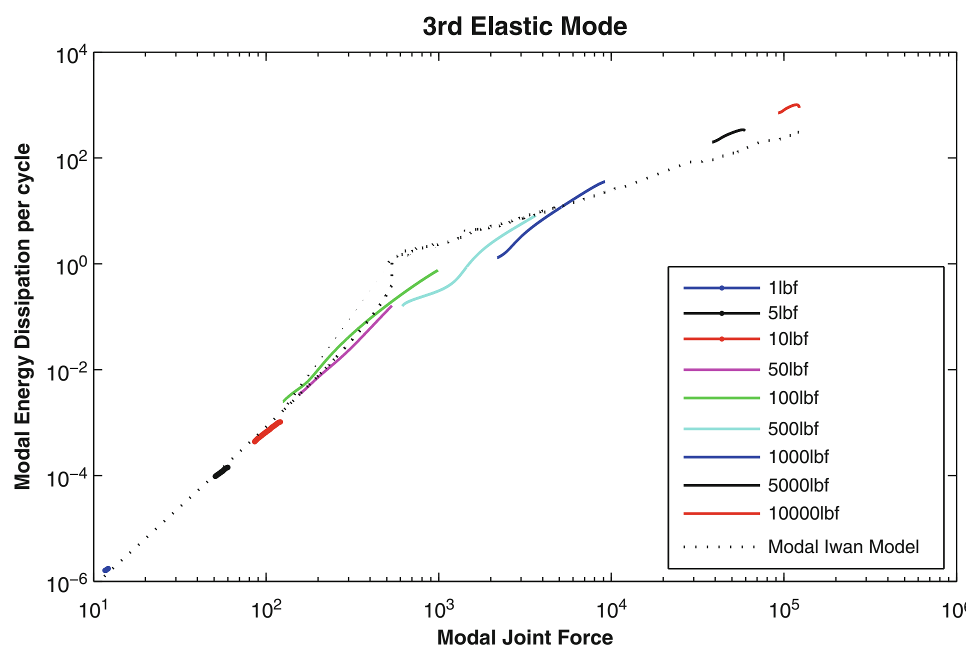

Fig. 2.11 Modal energy dissipation versus modal force for the 3rd elastic mode. The modal model agrees well with the discrete simulations for this mode in the micro-slip region, but not in the macro-slip region

The modal energy dissipation versus force for the second elastic mode is shown in Fig. 2.10. There are several interesting features in this plot. First notice how each simulation's energy dissipation seems to drop to essentially zero towards the end of each time record. Each time history was limited to 0.2 seconds due the small time step required and the large volume of data that was generated when each nodal time history was written to a file. Since there is an extremely small amount of damping in the 2nd bending mode, the fitted envelope has very little decay. Hence, the estimate of the energy dissipation is very sensitive to envelope fit by the Hilbert Transform algorithm. The slope of the modal Iwan model in Fig. 2.10 has a value of approximately 2 corresponding to a $\hat{\chi}$ value of -1 which is characteristic of a linearly damped system. Thus, the dissipation in this mode could be modeled with a linear mode and a linear modal damping ratio instead of a modal Iwan model. Apparently, the location of the link is such that the discrete Iwan joints are not exercised by this mode.

The comparisonin Fig. 2.11 shows that the deduced modal Iwan model for the 3rd elastic mode does a very good job of predicting the energy dissipation in the micro-slip region, for which a $\hat{\chi}$ value of $\hat{\chi}_3 = -0.048$ was obtained. This value indicates quite a strong dependence on force (recall that each discrete joint had $\chi = -0.3$. On the other hand, the modal Iwan model does a poor job of capturing the macro-slip region. The slope of the discrete Iwan simulations seems to be greater than the slope of the modal Iwan model in macro-slip. This suggests that Eq. (2.17) may not entirely describe the energy dissipation in the macro-slip region for this system. A similar effect was observed for some of the modes of the system studied in [5], the cause of which will be explored further in the future.

2.3.4.3 Discussion

These results validate the use of a modal Iwan model to capture the effect of discrete Iwan joints in the micro-slip region. On the other hand, the results suggest that the modal Iwan model may need to be modified to capture the response of a system at higher force levels corresponding to the macro-slip region. This is to be expected, perhaps, since the mode shapes used for the macro-slip region include joint stiffness; however, when the joints are in the macro-slip region the mode shapes should no longer include the joint stiffness. Also, the assumption of negligible modal interactions could very well be violated when the joints slip significantly.

2.4 Beam Experiments

The modal Iwan methodology was also assessed experimentally using experimental measurements from a free-free beam with a bolted link attached. The experimental setup was designed to minimize the effect of damping associated with the boundary conditions. Free boundary conditions were used because any other choice, e.g. clamped, would add significant damping to the system. In Sect. 2.4.5, the energy dissipation characteristics of the modal Iwan model are compared with those of the actual experiment.

2.4.1 Test Structure

The structure tested in this work was first used by Sumali in [17]. The beam was designed to have the following characteristics: the structure had numerous modes from 0–2000 Hz, the modes are well separated in frequency and the modes do not switch order when the links are attached. Previously, a washer was inserted between the link and the beam as was done for the finite element model in Fig. 2.6. Initial tests were done in this configuration but the damping in the joint seemed linear, indicating that there was no slip present in the joint for the force levels tested. The washers were then removed in order to spread out the clamping force between the beam and the connecting element. The resulting configuration is shown in Fig. 2.12. This change seemed to cause the joint to slip more easily, so a greater degree of nonlinearity was observed. Also, the bolt torque for the original experiments was set between 80 and 110 inch-pounds which results in bolt preload force of approximately 1600–2200 lbf. The bolt was tightened to a much lower torque of only 5 inch-pounds in these experiments.

The dimensions of the beam and link are the same as in the finite element model described in Sect. 2.3.1. However, there is no washer that separates the beam ($20'' \times 2'' \times 0.25''$) from the link ($3.5'' \times 0.5'' \times 0.125''$) as shown in Fig. 2.12. The bolts used to attach the link to the beam were $1/4''$-28 fine-threaded bolts. All components were made of AISI 304 stainless steel.

2.4.2 Lab Setup Challenges

The damping ratios of a freely supported structure are sensitive to the support conditions, as was explored in detail in [18]. Therefore, special attention must be given to the support conditions to assure that the damping that they add does not contaminate the results.

Fig. 2.12 Schematic of the link and beam connection that was used in the experimental setup

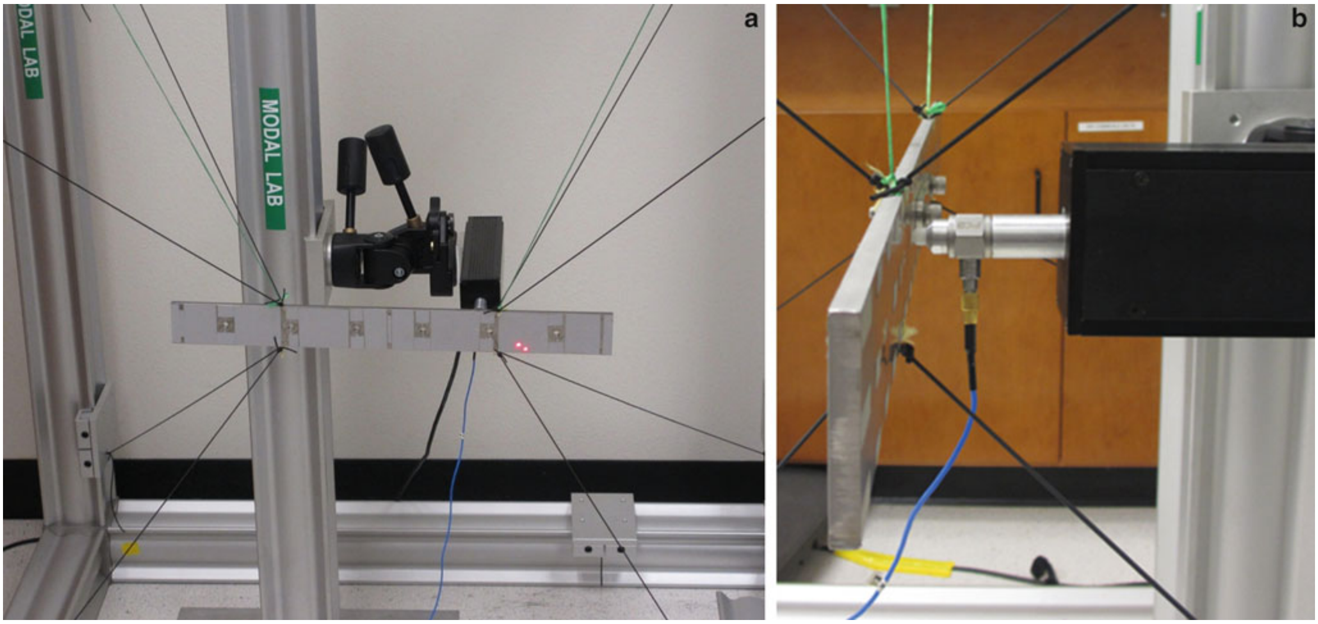

Fig. 2.13 Photograph showing how the beam was suspended (**a**). Automatic hammer positioned behind the impact point. One link is attached to the beam and can be seen behind the hammer (**b**)

Initially, the beam was suspended by two strings that act as pendulum supports as was done in [18]. To prevent the rigid body modes from contaminating the elastic mode data, the pendulum motion of the beam should have a low natural frequency compared to the first elastic mode. The general rule of thumb states that the error in the measured natural frequencies will be less than 0.5% when the rigid body natural frequencies are less than one tenth of the elastic natural frequencies of interest. However, that same design theoretically produces 10% error in the measured damping ratios. A frequency ratio of approximately 20 was obtained when the beam was supported by only these two strings. Although this test provided a good baseline that was used to evaluate the damping of the boundary conditions in subsequent tests, there were practical considerations that prohibited its use for most of the testing.

Specifically, the velocity of the beam was measured with a scanning laser Doppler vibrometer in order to eliminate any damping associated with the cables of contact sensors. Hence, if the beam swings significantly in its pendulum mode, the point which the laser is measuring may change significantly during the measurement. Also, an automated hammer was used to excite the beam, but the hammer only retracts about one inch after impact. As a result, the pendulum motion of the beam caused almost unavoidable double hits with this setup. Finally, in the processing described subsequently, it is important for the automatic hammer to apply a highly consistent impact force. Any swinging of the beam caused the impact forces to vary from test to test and it was extremely difficult and time consuming to try to manually eliminate the swinging. For these reasons, soft bungee cords were used to suppress the rigid body motion of the beam while attempting to add as little damping as possible to the system. The final set up was similar to that used in [17] and is shown in Fig. 2.13. This setup was used for all of the measurements shown in this paper.

2.4.3 Experimental Setup

The dynamic response of the beam was measured using a Polytec Scanning Laser Doppler Vibrometer (PSV-400) to measure the response at 54 points on the beam. A Polytec single point Laser Doppler Vibrometer (OFV-534) was used to measure a reference point to verify that the hammer hits were consistent. The reference laser was positioned close to the impact force location. An Alta Solutions Automated Impact Hammer with a nylon hammer tip was used to supply the impact force, which is measured by a force gauge attached between the hammer and the hammer tip.

The beam is suspended by 2 strings that support the weight of the beam and the 8 bungee cords prevent excessive rigid-body motion. The bungees and strings were connected to the beam at locations where the odd bending modes have little motion in order to minimize damping in those modes. However, even after all of the care that was taken, some damping was added by the supports. A preliminary analysis was done in which the damping ratios of the first few modes of the beam were measured with and without bungees, and the results are shown in Table 2.3.